

Quasi-two-dimensional frustrated spin-1 triangular lattice antiferromagnet $\text{Ca}_3\text{NiNb}_2\text{O}_9$: A proximate spin liquid

Sonia Deswal ^{1,*}, Deepu Kumar ¹, Dibyata Rout ², Surjeet Singh,² and Pradeep Kumar ^{1,†}

¹*School of Physical Sciences, Indian Institute of Technology Mandi, Mandi 175005, India*

²*Department of Physics, Indian Institute of Science Education and Research Pune, Pune 411008, India*



(Received 5 April 2024; revised 26 June 2024; accepted 8 July 2024; published 25 July 2024)

The spin-1 triangular lattice Heisenberg antiferromagnet $\text{Ca}_3\text{NiNb}_2\text{O}_9$ and its sister compounds are conjectured to promote the formation of many-body quantum entangled states such as a quantum spin liquid (QSL), an exotic phase which features fractionalized quasiparticle excitations and emergent gauges. We probe the single crystal of $\text{Ca}_3\text{NiNb}_2\text{O}_9$ using an in-depth Raman spectroscopic technique. Our measurements provide evidence for the fractionalized excitations, suggesting that the current system is in close proximity to the QSL phase. This is also in line with the proposed higher-order fractional magnetization plateau in this system, as these plateaus have an intricate relationship with the spin entanglement. We observed unconventional underlying scattering as a broad continuum with an intensity that shows fermionic statistics. Additionally, phonon modes show Fano asymmetry, also conjectured as a fingerprint of the spin-liquid phase, and above a critical Raman shift also show fermionic statistics in their intensity evolution.

DOI: [10.1103/PhysRevB.110.024430](https://doi.org/10.1103/PhysRevB.110.024430)

I. INTRODUCTION

Frustrated quantum antiferromagnets refer to the presence of competing exchange interactions that cannot be simultaneously satisfied. This phenomenon creates a large degeneracy in the ground state of the system [1–3]. The frustrated model has recently attracted much attention as a probable candidate for the highly entangled quantum spin-liquid (QSL) phase that can host non-Abelian quasiparticle excitations [4,5], and the exotic quasiparticle (QP) excitations known as spinons [6]. The most famous variant of QSL was proposed by Anderson [7], who emphasized the significance of frustration in stabilizing such phases like the resonating valence-bond (RVB) state for the spin- $\frac{1}{2}$ triangular-lattice antiferromagnet (TLAF) [7,8]. Experimentally, $S = \frac{1}{2}$ TLAFs have been and are under active investigation with no magnetic ordering observed down to very low temperatures and have been projected as potential QSL candidates [9–13]. TLAFs with small effective spin ($S = \frac{1}{2}$ or 1) display two competing ground states: one in which the spins are long-range ordered with 120° spin structure [14] [see Fig. 1(b)] and another in which the quantum fluctuations are expected to melt the long-range ordering, leading to RVB with a QSL ground state [15]. The change from a noncollinear 120° -spin configuration at zero magnetic fields into a fractional-magnetic lattice under a limited range of applied magnetic field, such as the collinear up-up-down phase corresponding to a plateau of magnetization with $\frac{1}{3}$ of its saturation value, aptly demonstrates the rich quantum phenomena that emerge in these systems [16,17]. We note that, so far, most studies have been focused on searching for

the QSL phase in the $S = \frac{1}{2}$ TLAF, and the $S = 1$ TLAF are largely unexplored. This is probably because the quantum fluctuations become less pronounced as the spin quantum number S increases according to the spin-wave theory for the simplest Heisenberg Hamiltonians. For identification of QSL candidates, one good indicator is the high value of frustration parameters $f = |\theta_{\text{CW}}/T_N|$, which indicates a strong suppression of ordering because of frustration. For the current system and its sister compounds, the frustration parameter ranges from 5 to 10 [14,18], which indicates moderate to high level of frustration due to competing interactions between the spins [1]. The recent studies on $S = 1$ TLAFs such as $\text{Ba}_3\text{NiNb}_2\text{O}_9$ [19] and $\text{Ba}_3\text{NiSb}_2\text{O}_9$ [20,21] have drawn attention due to the possible signature of a QSL phase manifested as fractional plateaus in the magnetization. Many other Ni^{2+} -based TLAF candidates have been proposed so far, but the direct confirmation of their QSL states remain elusive. Recently, for the case of a spin- $\frac{1}{2}$ kagome Heisenberg antiferromagnet, an intricate relation between $\frac{1}{9}$ magnetization plateau and spin entanglement [22] has been shown, suggesting a close link between the QSL phase and these magnetization plateaus.

The family of triple perovskites $A_3^{2+}(X^{2+}M_2^{5+})\text{O}_9$ has an ABO_3 structure with a 1:2 ordering of X and M ions at the B site, with the magnetic ions (X) arranged on vertices of a triangular lattice. Here, $\text{Ca}_3\text{NiNb}_2\text{O}_9$ is a member of the triple perovskite family. The triangular layers of Ni cations (NiO_6 oxygen octahedron) are separated by the double nonmagnetic corner-shared Nb_2O_{11} perovskite in the ab plane [see Fig. 1(c)] [23,24]. Also, $\text{Ca}_3\text{NiNb}_2\text{O}_9$ exhibits long-range ordering with two successive phase transitions at $T_{N1} = 4.6\text{K}$ and $T_{N2} = 4.2\text{K}$ (having Curie-Weiss temperature $\theta_{\text{CW}} = -23\text{K}$), with a 120° antiferromagnetic spin structure as the ground state. Such behavior implies strong

*Contact author: Soniadeswal255@gmail.com

†Contact author: pkumar@iitmandi.ac.in

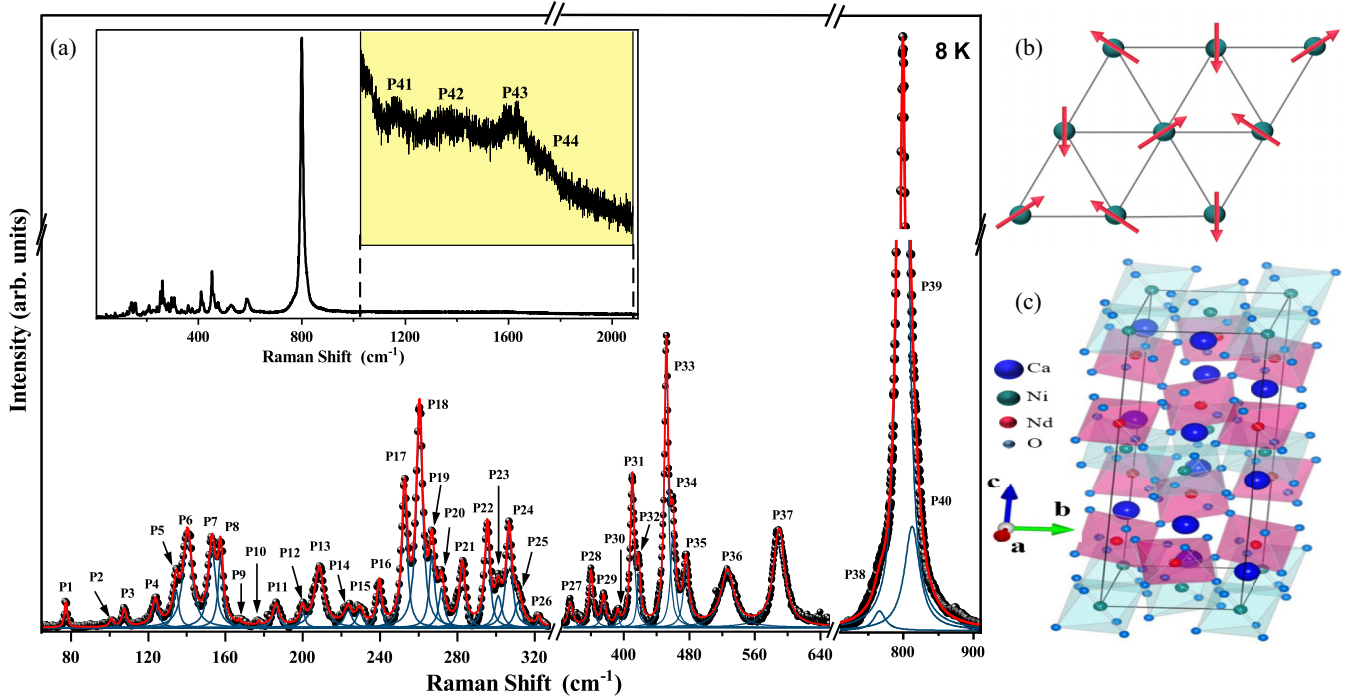


FIG. 1. Unpolarized Raman spectra of the single crystal of $\text{Ca}_3\text{NiNb}_2\text{O}_9$ in the spectral range of $65\text{--}910\text{ cm}^{-1}$ collected at 8 K using 532 nm laser excitation. The solid thick red line is a total sum of Lorentzian fit of the experimental data, and solid thin blue lines correspond to the individual Lorentzian fit of the phonon modes. The observed modes are labeled as P1–P40. Inset shows the raw spectrum for the spectral range of $10\text{--}2100\text{ cm}^{-1}$. The spectra in the yellow background are the amplified for the range of $910\text{--}2100\text{ cm}^{-1}$, showing very weak modes labeled as P41–P44. (b) Below T_{N1} ($\sim 4.6\text{ K}$), a 120° ordered ground state magnetic structure formed by Ni^{2+} spins at zero magnetic field. (c) The lattice structure with the Ni-triangular lattice of $\text{Ca}_3\text{NiNb}_2\text{O}_9$, plotted using VESTA, the solid-black line denote the unit cell.

geometrical frustration in the triangular lattice, suggesting the possibility of spin-liquid phases [18]. It is worth noting that frustration parameter f , which is 5 for $\text{Ca}_3\text{NiNb}_2\text{O}_9$, indicates a moderate to high degree of frustration and competitive interaction. We note that most potential QSL designated systems tend to show long-range magnetic ordering at low temperature. The spin-liquid state is preempted by this long-range ordering. However, despite this, the signature of a possible QSL may be gauged from the anomalous signature of the QP excitations even at much higher temperatures than T_N [25–28]. The general form of a quasi-two-dimensional (2D) XXZ Heisenberg Hamiltonian that captures the physics of TLAf systems can be written as [14,29] $H = J \sum_{\langle i,j \rangle}^{\text{layer}} (S_i^x S_j^x + S_i^y S_j^y + \Delta S_i^z S_j^z) + J' \sum_{\langle l,m \rangle}^{\text{interlayer}} S_l \cdot S_m$, where J and J' ($J'/J = 0.31$, for $\text{Ca}_3\text{NiNb}_2\text{O}_9$) are the intralayer and interlayer nearest-neighbor (NN) antiferromagnetic exchange energies, respectively [14,30]. Here, Δ ($0 < \Delta \leq 1$) is the 120° structure easy-plane exchange anisotropy. Spectroscopic studies on $\text{Ca}_3\text{NiNb}_2\text{O}_9$ for understanding the dynamics of underlying QP excitations are lacking. Inelastic light scattering, Raman in particular, is an excellent tool for investigating the exotic QP excitations such as spinons, triplons [31], and Majorana fermions [32,33], a defining feature of non-Abelian quantum statistics with intricate coupling between spin and lattice degrees of freedom [34,35]. Using Raman spectroscopy, bimagnon excitations have been reported in the distorted TLAf $\alpha\text{-SrCr}_2\text{O}_4$ [36] and a broad continuum with

distinct characteristic attributed to the spin-fractionalized excitations like spinons [26,37,38].

Motivated by the possible rich underlying QP excitations in these TLAf systems due to their close proximity to the QSL state, we carried out an in-depth investigation of B -site ordered single crystals of spin $S = 1$ TLAf $\text{Ca}_3\text{NiNb}_2\text{O}_9$ via inelastic light scattering, i.e., Raman scattering. In this paper, we reveal an intriguing magnetic scattering in this system, which is characterized by the presence of a broad continuum and Fano asymmetries in the phonon line shapes, suggesting proximity to the QSL phase. We observed strong anomalies in the self-energy parameters of the phonons (i.e., frequencies and linewidth) at $\sim 50\text{ K}$ (T_{SC} = short-range spin-spin correlation transition temperature) much higher than the long-range magnetic ordering temperature ($T_N \sim 4\text{ K}$), which suggest these anomalies do not arise from the conventional spin-phonon coupling, as the spins are deep inside the thermal paramagnetic regime with $\langle S_i \rangle = 0$. We attribute these anomalies in the phonons to the quantum spin and orbital fluctuations and possible coupling with the Majorana fermions. We also observed changes in the phonons self-energy parameters in the vicinity of $\sim 200\text{ K}$ (T^*).

II. RESULTS AND DISCUSSION

A. Raman scattering

A single crystal of B -site ordered $\text{Ca}_3\text{NiNb}_2\text{O}_9$ was crystallized into the monoclinic structure with space group $P12_1/c_1$

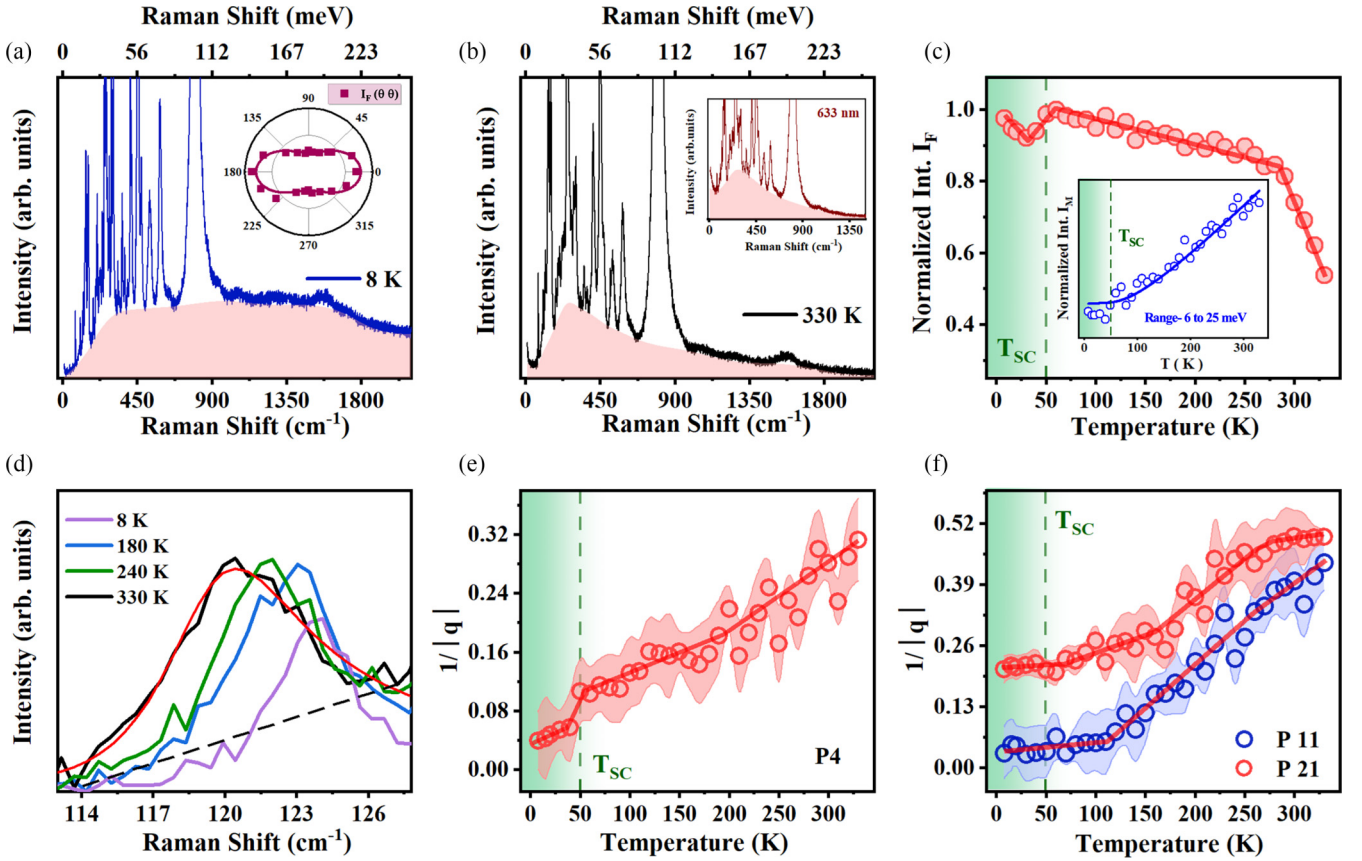


FIG. 2. The shaded background continuum at (a) 8 K and (b) 330 K, using 532 nm laser. Inset in (a) shows the integrated intensity of the continuum for $(\theta\theta)$ configuration reflecting A_g symmetry, and inset in (b) shows the background continuum using 633 nm at 330 K. (c) Normalized integrated intensity (I_F) for the full range (1.2–260 meV). The inset shows the background temperature variation of integrated intensity for low-energy range 6–25 meV, the blue line is the fitted curve by Bosonic function as discussed in the text. (d) Temperature evolution of asymmetry of mode P4, solid red line shows the Breit-Wigner-Fano (BWF) fit. Temperature evolution of the asymmetry parameter $1/|q|$ of mode (e) P4, (f) P11 and P21; the error bars are shown by fill area around the datasets. The solid red lines are a guide to the eye.

(#14) and the point group C_{2h} . Factor group analysis gives 180 phonon branches at the Γ point of the Brillouin zone given by the following irreducible representation $\Gamma_{\text{Total}} = 42A_g + 48A_u + 42B_g + 48B_u$. Out of these, 93 are infrared active $\Gamma_{\text{IR}} = 47A_u + 46B_u$, and 84 are Raman active $\Gamma_{\text{Raman}} = 42A_g + 42B_g$, and the remaining three correspond to the acoustic phonons $\Gamma_{\text{Acoustical}} = A_u + 2B_u$ [39] (see Table S1 in the Supplemental Material [40] for more details). The unpolarized Raman spectrum of $\text{Ca}_3\text{NiNb}_2\text{O}_9$ at 8 K using 532 nm laser excitation is shown in Fig. 1(a), covering a spectral range from 65 to 910 cm^{-1} . To extract the mode frequency (ω), full width at half maximum (FWHM), and intensity of each individual mode, the spectrum at each temperature is fitted with a sum of Lorentzian functions, allowing us to distinguish 40 phonon modes that have been labeled as P1–P40 for convenience. Peak positions of the observed phonons at 8 and 330 K are listed in Table S2 in the Supplemental Material [40]. The inset in Fig. 1(a) shows the Raman spectrum collected up to 2100 cm^{-1} , showing four very weak peaks (P41–P44) in the frequency range of 900–2100 cm^{-1} attributed to the second-order Raman scattering. It has been observed that mode P39 centered at $\sim 800 \text{ cm}^{-1}$ is almost 6–8 times more intense than the other modes [see the inset in Fig. 1(a)] and has its origin in the stretching of oxygen octahedra [41]. The

tentative symmetry assignment of the phonon modes based on our polarization-dependent Raman measurements is described in Sec. S4 in the Supplemental Material [40]. We also undertake comparative Raman analyses for both B -site ordered and disordered samples (see Sec. S3 in the Supplemental Material [40]). The Raman spectra of the B -site ordered $\text{Ca}_3\text{NiNb}_2\text{O}_9$ demonstrated two unusual features: the occurrence of the broad continuum and the anomalous temperature dependency of the phonon modes. In the following, we discuss both these observations in detail.

B. Evolution of the underlying quasiparticle excitations

Raman spectra of $\text{Ca}_3\text{NiNb}_2\text{O}_9$ at 8 and 330 K [see Figs. 2(a) and 2(b)] with phonon modes overlaid on a wide temperature-dependent continuum (shown as red shading) ranging up to 260 meV are assigned to the underlying magnetic excitations. To rule out its origin due to fluorescence, we also did measurements using different laser energies [see inset of Fig. 2(b)] and found that the continuum intensity shows no significant laser energy dependence, reflecting its intrinsic nature and not due to fluorescence. Generally, the continuum observed in the Raman measurements may have its origin in the magnetic excitations, electronic excitations, e.g.,

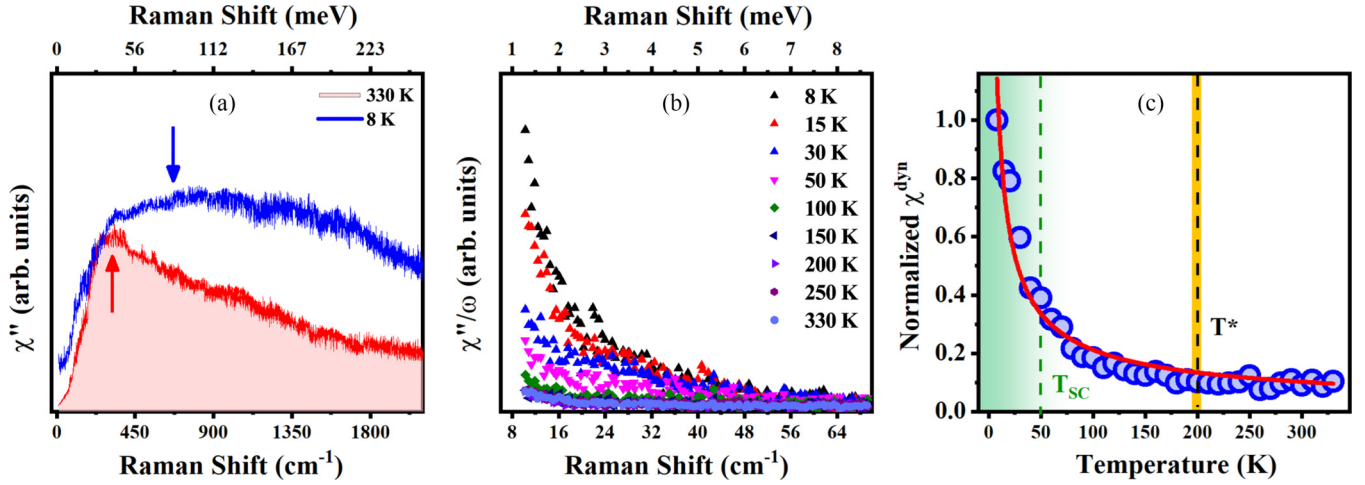


FIG. 3. (a) Comparison of the phonons subtracted Raman response $\chi''(\omega, T)$ at 8 and 330 K. The arrows mark the local maximum for the spectral weight. (b) Temperature evolution of the phonons subtracted Raman conductivity $\chi''(\omega, T)/\omega$ in the low-frequency range of 1.2–8 meV. (c) Temperature dependence of the dynamic spin susceptibility, obtained from the Kramers-Kronig relation $\chi^{\text{dyn}} \equiv \frac{2}{\pi} \int_0^{8\text{meV}} \frac{\chi''(\omega)}{\omega} d\omega$. The solid red line is the fitted curve with the power law $\chi^{\text{dyn}}(T) \propto T^\beta$.

charge transfer excitations, plasmonic excitation (generally if material is metallic in nature), and some time disorder in the sample or thermal fluctuations. The continuum increases with decreasing temperature down to the lowest recorded temperature, i.e., 8 K, see Fig. 3(a). It is noteworthy that thermal fluctuations decrease with decreasing temperature; hence, the continuum cannot be attributed to the thermal fluctuations. Since the sample probed is a single crystal and shows very sharp phonon modes, it declines the cause of continuum due to disorder. Internal charge transfer excitations (electronic in nature) are a few times broader than a typical phonon mode, typically having linewidth $\sim 100\text{--}200\text{ cm}^{-1}$, but the observed continuum is spread over a much broader range; hence, its charge transfer electronic transition nature may be ruled out as well. The quantum magnetic nature and underlying frustration of $\text{Ca}_3\text{NiNb}_2\text{O}_9$ may lead to exotic spin dynamics and quasiparticle excitations, potentially manifesting as a broad continuum in the Raman spectrum. A comparison of the 8 and 330 K curves reveals that the continuum shape shows strong variation with temperature. This continuum with a maximum at $\sim 83\text{ meV}$ ($\sim 670\text{ cm}^{-1}$) is observed for 8 K; as temperature rises, the continuum becomes narrow and redshifts and shows maxima at $\sim 40\text{ meV}$ ($\sim 320\text{ cm}^{-1}$) for 330 K. The quantitative estimate of this continuum temperature dependence is elucidated via integrated intensity $I_F = \int_{\omega_l}^{\omega_h} I(\omega) d\omega$ in the acquired full-spectrum range, where the cutoffs ω_l and ω_h are taken at 1.2 and 260 meV, respectively [see Fig. 2(c)]. A higher-frequency range for I_F is chosen until the maximum recorded spectrum range. In the low-temperature ($T < T_{\text{SC}} \sim 50\text{ K}$) regime, I_F shows small change; however, at T_{SC} , it shows a sharp change, and after that, a monotonous decrease is observed until $T^* \sim 200\text{ K}$. The continuum loses its intensity above T^* and reaches at its minimum value $\sim 330\text{ K}$, with a broad peak at the low-frequency region. The overall temperature evolution of the intensity follows fermionic statistics, suggesting the spinon nature of these underlying excitations, as also seen in the phonon-mode intensity evolution (discussed in Sec. III). The inset of Fig. 2(c) shows the

integrated intensity I_M of the spectral weight in the energy window ($6 < \omega < 25\text{ meV}$). We took this higher range $\sim 25\text{ meV}$ ($\sim 203\text{ cm}^{-1}$), which marks the demarcating frequency below and above which phonon modes are showing opposite behavior. It exhibits a pronounced temperature dependency, as expected for one/two-particle scattering governed by the thermal Bose factor $1 + n(\omega_b) = 1/[1 - \exp(-\hbar\omega_b/k_B T)]$ at temperature above $\sim 40\text{ K}$, with fitted parameter $\omega_b = 23 \pm 1.2\text{ meV}$ extracted from the bosonic fit. Interestingly below $\sim 40\text{ K}$, it shows increasing behavior reflecting the fermionic contribution to the intensity at low temperature. The observed A_g symmetry [see the inset of Fig. 2(a)] of the continuum (as inferred from the two-lobe structure, see Sec. S4 in the Supplemental Material [40] for more details on the polarization measurements) indicates a distinct topology of the underlying excitations. We note that Raman susceptibility approaches zero as the frequency (Raman shift) goes to zero, i.e., $\chi'' \propto \omega$ [see Fig. 3(a)], suggesting the gapless nature of these underlying excitations. The observation of a broad continuum at temperatures surpassing T_N hints at its association with the strong quantum fluctuations and magnetic frustration [42]. We note that such an anomalous continuum of underlying QP excitations has been attributed to the fractionalized spin (spinons) as well as one/two-pair spinon-antispinon excitations in different magnetic quantum systems [43–45]. Experimental as well theoretical studies on a sister compound $\text{Ba}_3\text{NiSb}_2\text{O}_9$ have revealed the signature of fermionic spinons attributed to the exotic gapless QSL state [46–48]. The continuum we observed in our case suggests its origin in the spin fractionalization, which arises from the frustration of Ni^{2+} spins forming a triangular lattice. Our observation of the anomalous background continuum and anomalous phonon mode intensity temperature evolution suggests that $\text{Ca}_3\text{NiNb}_2\text{O}_9$ is in close proximity to the gapless QSL phase.

Interestingly, several phonons (e.g., P4, P11, and P21) exhibit asymmetric Fano line shape on top of the magnetic continuum. This asymmetric nature indicates quantum

interference of the discrete states (phonons here) with the underlying excitations responsible for the continuum and may provide information about the nature of the underlying QP excitations responsible for the magnetic continuum. Recently, it has been advocated theoretically for the QSL candidates that spin-phonon coupling renormalizes phonon propagators and generates the Fano line shape, resulting in the observable effect of the Majorana fermions and the Z2 gauge fluxes [49,50]. This conjecture of Fano line asymmetry in the phonon modes is supported by the experimental observations in putative QSL candidates [26,51–53], suggesting the intimate link between the phonon asymmetric line shape and the QSL state. The P4 phonon mode [see Fig. 2(d)] is fitted with the Breit-Wigner-Fano profile [54] $I_{\text{BWF}}(\omega) = I_0[1 + (\omega - \omega_c)/q\Gamma]^2 / [1 + ((\omega - \omega_c)/\Gamma)^2]$, where ω , ω_c , and Γ are the Raman shift, spectral peak center, and FWHM, respectively [55], and q is the asymmetry parameter that characterizes the coupling strength with the continuum, quantified by the parameter $1/|q|$. Microscopically, q is inversely proportional to V_E , and V_E tells the interaction between discrete state and the continuum. Therefore, in the limit $1/|q| (\propto |V_E|) \rightarrow \infty$, coupling is stronger and results in a more asymmetric peak, while in the limit $1/|q| \rightarrow 0$, coupling is weak, and the line shape gravitates toward Lorentzian. Figures 2(e) and 2(f) show the temperature dependence of the coupling strength ($1/|q|$) for the Fano peak (P4, P11, and P21) in the temperature range of 8–330 K. We note that, with lowering temperature, $1/|q|$ decreases continuously, indicating an intimate link with the underlying continuum behavior in the frequency range of ~ 6 –48 meV (see Fig. S7 in the Supplemental Material [40]). Below $T_{\text{SC}} (\sim 50 \text{ K})$, it remains constant for modes P11 and P21; however, for mode P4, it shows a sharp drop. Generally, the asymmetry ($1/|q|$) should be more pronounced with decreasing temperature, as asymmetry in the phonon modes is also expected in the spin-liquid phase. We note that asymmetry in the phonon modes for the current system certainly decreases with decreasing the temperature, but the magnitude of asymmetry is quite appreciable ~ 0.05 – 0.2 around 50 K, e.g., the asymmetry magnitude for the putative QSL system is in the range of ~ 0.08 – 0.15 around 50 K [45,51,56]. The opposite trend in $1/q$ as compared with other putative QSL candidates may have its origin in the nature of the underlying continuum in the frequency range of ~ 6 –48 meV, which shows increasing behavior with increasing temperature (see Fig. S7 in the Supplemental Material [40]). Consequently, phonon modes P11, P14, and P21 overlapping with this continuum may result in a more asymmetric nature at higher temperatures.

C. Dynamic spin susceptibility

In Fig. 3(a), we present the phonon-subtracted Raman response $\chi'' \propto I(\omega)/[1 + n(\omega)]$ continuum extending up to 260 meV, which shows the underlying dynamic collective excitations at a given temperature. Interestingly, the Raman response shows a significant temperature dependence in the spectral weight upon lowering the temperature [see Figs. 2(c) and 3(a)]. Upon warming, the continuum starts to narrow and changes its position of maximum. For 330 K, it shows a maximum at ~ 40 meV, and it shifts to ~ 83 meV at 8 K. For

further probing the evolution of this continuum, we quantitatively evaluated χ^{dyn} , shown in Fig. 3(c), in the low-frequency regime. The low-energy Raman conductivity χ''/ω shows a pronounced peak about $\omega = 0$, which becomes stronger with decreasing temperature, see Fig. 3(b). We evaluated the dynamic spin susceptibility χ^{dyn} using the Kramers-Kronig relation [32]: $\chi^{\text{dyn}} = \lim_{\omega \rightarrow 0} \chi(k=0, \omega) \equiv \frac{2}{\pi} \int_0^{\Omega} \frac{\chi''(\omega')}{\omega'} d\omega'$, associated with the low-energy measurement, from 1.2 to 8 meV. It exhibits sharp increase below $T_{\text{SC}} (\sim 50 \text{ K})$, signifying the building of the short-range ordering much above $T_N (\sim 0.08T_{\text{SC}})$. We note that $\chi^{\text{dyn}}(T)$ is nearly constant from 330 to ~ 200 K (T^*), as expected in the pure paramagnetic phase, and starts rising below it, signaling building up of the spin-entangled phase. The relative change in $\chi^{\text{dyn}}(T)$ in the temperature range of 330–200 K is 1% with respect to its value at 330 K; at 200 K to T_{SC} (50 K), it increases by $\sim 29\%$ with respect to its value at 200 K; and from T_{SC} to the lowest recorded temperature (8 K), it increases by $\sim 61\%$ with respect to its value at 50 K. Here, $\chi^{\text{dyn}}(T)$ divergence behavior as $T \rightarrow 0$ K hints at the dominating nature of quantum fluctuations associated with the underlying collective excitations. Our observations are also in line with the theoretical proposals, where it had been suggested that the dynamic correlations may have distinct temperature evolution in systems with QSL signatures, and the fractionalization of the quantum spins contributes to the dynamic spin fluctuations even in the high-temperature paramagnetic phase [57]. Therefore, spin-fractionalization signatures are expected in the dynamical measurable properties such as $\chi^{\text{dyn}}(T)$, as observed here. Also, $\chi^{\text{dyn}}(T)$ may be described by the power law given as $\chi^{\text{dyn}} \propto T^\beta$ ($\beta = -0.65 \pm 0.04$). We observed the power-law behavior of $\chi^{\text{dyn}}(T)$ much above T_N , unlike the conventional pure paramagnetic phase, where it is expected to show saturation, suggesting slowly decaying correlations inherent to a spin-liquid state [58]. Experimentally, the possibility of higher-order plateaus is suggested at $\frac{\sqrt{3}}{3}$ or $\frac{3}{4}$ [18], indicating the involvement of entangled spins. It is worth mentioning that, in addition to the anomalous phonons and broad underlying continuum, the temperature dependence of $\chi^{\text{dyn}}(T)$ in $\text{Ca}_3\text{NiNb}_2\text{O}_9$ is very similar to that of other putative QSL candidates [27,28,56,59]. Our observations suggest the presence of excitations which are intimately linked with the QSL state in this spin-1 frustrated triangular antiferromagnet $\text{Ca}_3\text{NiNb}_2\text{O}_9$. This is also in line with the theoretical proposals and experimental observation on sister compounds [9,46,47].

III. TEMPERATURE AND POLARIZATION DEPENDENCE OF THE PHONON MODES

Figure 4(a) shows the Raman spectrum from 90 to 330 cm^{-1} at a few temperatures. It illustrates interesting changes that are described in the following. With increasing temperature, we observed a dramatic gain in intensity of the Raman modes > 50 K. Moreover, the spectral weight flips at a demarcating Raman shift $\omega_F \sim 203 \text{ cm}^{-1}$, i.e., the phonon modes above and below ω_F exhibit opposite behaviors in their intensity evolution from ~ 50 to 330 K [see color plot in Figs. 4(b) and 4(c)]. Based on the demarcating frequency

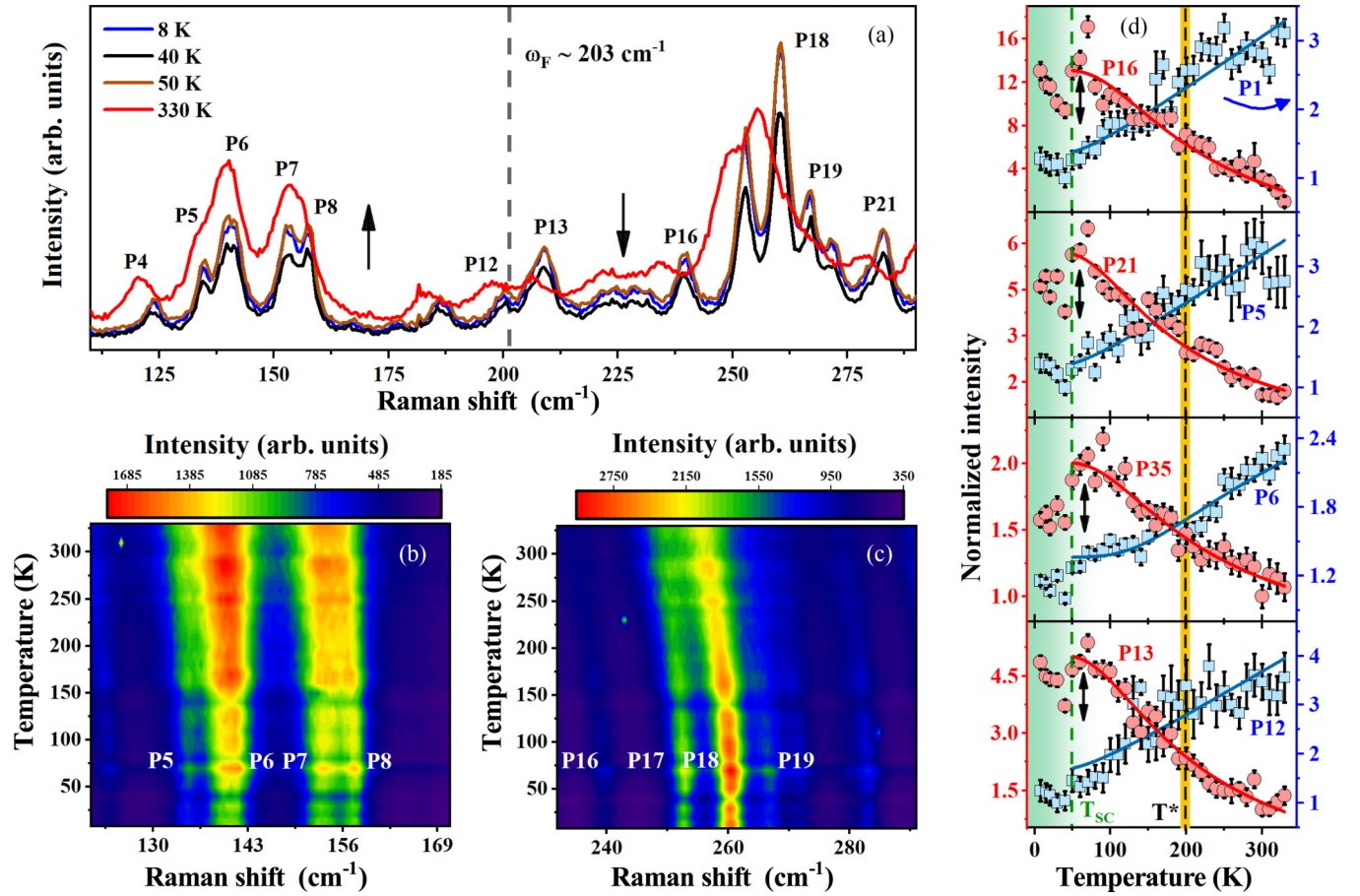


FIG. 4. (a) Temperature evolution of the Raman spectrum in the spectral range of 90–330 cm^{-1} at 8, 40, 50, and 330 K. The downward/upward arrows indicate the decrease/increase in the Raman intensity with increasing temperature, respectively. (b) Color contour map of the Raman intensity vs Raman shift as a function of temperature for the few phonon modes (P5, P6, P7, and P8) below $\omega_F \sim 203 \text{ cm}^{-1}$ and (c) for the few phonon modes (P16, P17, and P19) above ω_F . Modes below ω_F show higher intensity at higher temperature; on the other hand, modes above ω_F show lower intensity at higher temperature. (d) Temperature-dependent integrated intensity for the few selected phonon modes above and below ω_F . The solid red and blue lines are the fitted curves using the equation as described in text. Double-sided arrows are a guide to the eye to show sharp jumps in the intensity of the phonon modes ~ 50 K.

ω_F , we categorize the phonon modes into two groups: P1–P12 encompass the lower energy modes, while P13–P40 denote the higher-energy modes. Most of the observed modes (modes from lower as well as higher sides of ω_F) exhibit an anomalous intensity decrease with warming up toward 40 K (i.e., mode intensity decreases with increasing temperature), followed by a sharp jump at ~ 50 K. Thereafter, the intensity goes on increasing for the low-energy modes corresponding to the region $\omega < \omega_F$ but shows a decreasing behavior for the modes in the region $\omega > \omega_F$. Generally, as the phonons are bosons, one expects the temperature evolution of phonons to obey the Bose-Einstein statistics, i.e., mode intensity is expected to increase with increasing temperature. Figure 4(d) illustrates the normalized integrated intensity of some of the low-frequency modes P1, P5, P6, and P12. For these modes, intensity enhances roughly by a factor of three between ~ 50 and 330 K. This follows the conventional temperature dependence caused by thermal Bose factors $[1 + n(\omega)]$, where $n(\omega, T) = 1/[\exp(\hbar\omega/k_B T) - 1]$, in line with the elevated populations of phonons with increasing temperature [60]. Surprisingly, this is not the case for the high-energy phonon modes above ω_F ,

see Fig. 4(d) for modes P13, P16, P21, and P35. They exhibit a completely opposite behavior from the conventional one, i.e., their intensity decreases upon increasing the temperature from ~ 50 to 330 K. Being in stark contrast with bosonic nature, high-energy modes follow the fermionic statistics, and as shown in Fig. 4(d), their intensity variation with temperature can be well fitted to the two-fermion functional related to the creation and annihilation of a pair of fermions, given as $A + B[1 - f(\omega)]^2$, where $f(\omega) = 1/[\exp(\hbar\omega/k_B T) + 1]$ is the Fermi distribution function with zero chemical potential [32]. This unconventional observation hints at the fractionalized nature of the underlying QP excitations analogous to that reported for the case of spin-liquid systems. Recently, it was also proposed for the $S = 1$ antiferromagnets in 2D that there exists deconfinement of spinon and holon excitations with non-Abelian statistics [61]. For a simplistic picture, we have used the two-fermion functional relation to fit the phonon-mode intensity above the demarcating frequency (ω_F). As phonons are bosons and a higher-order phonon decays into lower-energy phonons, their temperature-dependent intensity is generally governed by the Bose statistics. However, for

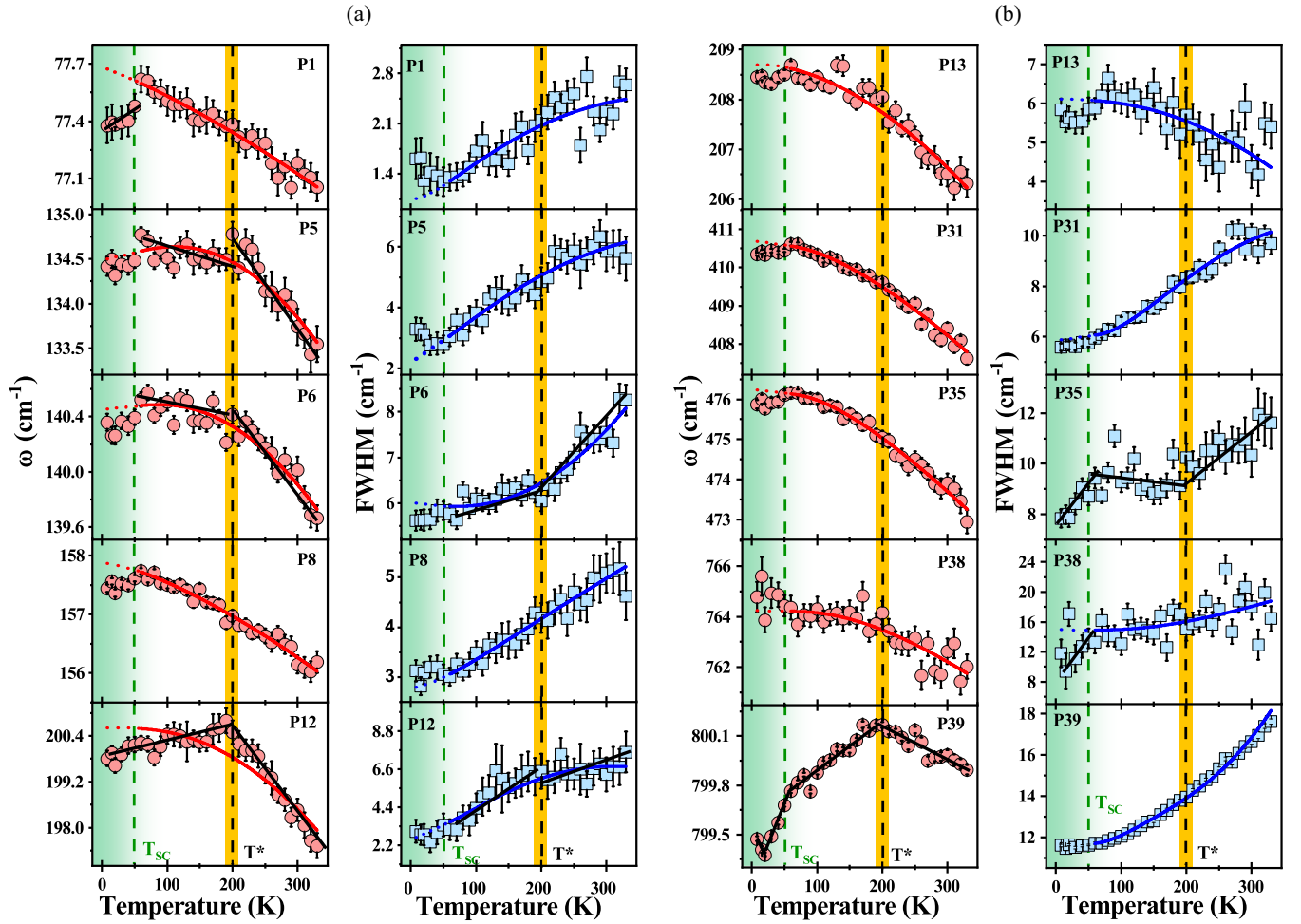


FIG. 5. (a) and (b) Temperature variation of the mode frequency and line width [full width at half maximum (FWHM)] of the phonon modes above and below the demarcating Raman shift $\omega_F \sim 203 \text{ cm}^{-1}$, respectively. The solid red and blue lines are the fitted curves using the equation as described in Sec. S2 in the Supplemental Material [40], and broken lines are the extended estimation of fitted curves. The black solid lines are a guide to the eye. The green shaded region illustrates the anomalous behavior below $T_{SC} \sim 50 \text{ K}$, while yellow shades indicate the deviation in slope of the curve around $T^* (\sim 200 \text{ K})$.

the spin-liquid systems, a phonon may decay into Majorana fermions; therefore, its intensity evolution may be governed by the two-fermion model, as suggested for Kitaev QSL systems [32]. However, there is a caveat that strictly this two-fermion functional was originally derived for a hexagonal honeycomb system with spin $S = \frac{1}{2}$, and the current system is a triangular lattice with $S = 1$. We hope our studies will provide motivation to explore the frustrated triangular lattice system in this direction theoretically.

Generally, materials show frequency softening and linewidth broadening of the phonon modes due to increased anharmonic thermal vibration on warming [60,62]. Figures 5(a) and 5(b) showcase temperature evolution of the mode frequency and FWHM for some of the strongest modes (see Fig. S2 in the Supplemental Material [40] for other modes). The following important observations can be made: (i) Most of the phonon modes exhibit anomalous frequency decrease with decreasing temperature below $\sim 50 \text{ K}$ (T_{SC} , defined as the spin-spin correlation temperature) down to the lowest recorded temperature, i.e., 8 K in our experiments. (ii) Interestingly, for the phonon modes (P5, P6, P12, and

P39), the frequency exhibits a subtle kink/change in slope in the vicinity of $\sim 200 \text{ K}$ and, after that, shows normal behavior until 330K. (iii) The temperature-induced frequency shift $\Delta\omega_{T_{SC}-330\text{K}}$ for the low-energy phonon modes (below ω_F) are $\sim 0.5\text{--}2.5 \text{ cm}^{-1}$, while the high-frequency modes (excluding the P39 mode) demonstrate a substantial frequency shift $\sim 2\text{--}8 \text{ cm}^{-1}$. The different normalizations of the phonon modes may be due to different symmetries of modes and amplitudes of the lattice vibrations [63]. Additionally, two very weak modes P38 ($\sim 765 \text{ cm}^{-1}$) and P40 ($\sim 813 \text{ cm}^{-1}$) appear as the shoulders of the most intense mode P39, as shown in Fig. S1(a) in the Supplemental Material [40]. This may be due to the local symmetry change, as Raman is very sensitive to any local symmetry distortions. Their frequencies and linewidth also show change in slope at T_{SC} ($\sim 50 \text{ K}$). The frequency of the P39 mode shows anomalous behavior from 8 to $\sim 200 \text{ K}$, i.e., hardening with increasing temperature until $\sim 200 \text{ K}$, see Fig. 5(b). This anomalous behavior may have its origin in the strong phonon-phonon anharmonic interactions [63,64].

Further, we discuss the phonon linewidth. The following observation can be made: (i) Linewidths (FWHM) of all the

modes show normal behavior, i.e., FWHM decreases with decreasing temperature, from 330 K to T^* (~ 200 K). (ii) For modes P6, P12, and P35, the linewidths show a change in slope in the vicinity of T^* . (iii) For modes P1, P5, P8, P12, and P19, the linewidths show an anomalous broadening below T_{SC} (~ 50 K); on the other hand, P13, P35, and P38 show narrowing below T_{SC} . (iv) As for mode P13, it also shows anomalous behavior, i.e., linewidth increases with decreasing temperature from 330 K to T_{SC} . The increase in linewidth below T_{SC} suggests the decreased lifetime (τ) of the phonons ($\tau \propto 1/\text{FWHM}$), and this may happen due to the emergence of underlying quasiparticle excitations, providing an additional decay channel to the phonon modes. For the present system, it is possible that strong quantum spin fluctuations start coming into picture. Though T_N (~ 4 K) is much less than T_{SC} , the renormalization reflects strong quantum spin fluctuations in the paramagnetic state. We note that the Curie-Weiss temperature for $\text{Ca}_3\text{NiNb}_2\text{O}_9$ is ~ 23 K, which is also lower than T_{SC} [18]. The absence of any anomaly in the bulk measurements such as specific heat or magnetization around this temperature further suggests that this temperature corresponds to the limit below which the quantum spin fluctuations began to dominate.

Most of the modes (except the frequency increase of P39 and P12) show normal behavior in frequency-temperature evolution, i.e., frequency decreases with increasing temperature from ~ 50 to 330 K. The frequency and FWHM of most of the phonon modes in the temperature range of ~ 50 –330 K may be understood by considering the cubic and quadratic anharmonicity effect, as proposed by Klemens [65]. These are described in detail in Sec. S2 in the Supplemental Material [40]. The anomalous behavior of the phonons below T_{SC} (~ 50 K) cannot be captured by the anharmonic model, indicating involvement of some other degrees of freedom in the low-temperature regime. The spin-phonon coupling, a crucial parameter for magnetic materials, may give rise to anomalous softening and broadening of phonons in the temperature regime below the long-range magnetic ordering temperature. However, in the present case, the role of direct spin-phonon coupling on the phonon modes may be ruled out or is minimal since the long-range magnetic ordering temperature for $\text{Ca}_3\text{NiNb}_2\text{O}_9$ is much less than T_{SC} . It suggests that anomalies below $T_{SC} \sim 50$ K may derive from the strong quantum spin fluctuations or an effect of entering of the system from paramagnetic to the correlated paramagnetic phase. Here, $\text{Ca}_3\text{NiNb}_2\text{O}_9$ exhibits competing ferro- and antiferro-orbital fluctuations [14]. Renormalization of the phonons self-energy around T_{SC} may be associated with the spin and orbital fluctuations. We note that, recently, a strong orbital fluctuation along with spins has been reported for a quantum magnet via anomalies observed in the phonon self-energy parameters [66]. We note that renormalization of the phonon modes starts much above T_N , and this may be captured quantitatively by the spin and orbital fluctuations. As it is well understood, below T_N , considering the simplest NN Heisenberg Hamiltonian: $H \propto J_{ij}\mathbf{S}_i\mathbf{S}_j$, where J_{ij} represents spin-spin exchange interactions, the phonon renormalization is proportional to the spin-spin correlation function, i.e., $\Delta\omega \propto \langle \mathbf{S}_i\mathbf{S}_j \rangle$ [67]. Generally, the i th spin may be given as $\mathbf{S}_i \propto \mathbf{M} + \Delta\mathbf{S}_i$, where \mathbf{M} is the average sublattice magnetization per Ni^{2+} ion and

is zero above T_N , and $\Delta\mathbf{S}_i$ is the quantum spin fluctuation which exists at all temperatures. Above T_N , in the paramagnetic phase, \mathbf{M} is zero; hence, only the spin-fluctuation term will survive, i.e., phonon renormalization may be due to the term $\langle \Delta\mathbf{S}_i\Delta\mathbf{S}_j \rangle$, as spin fluctuation exists even in the paramagnetic phase. Similarly, if the orbitals are also active, in the present case, Ni e_g orbitals, then the Hamiltonian may be modified as $H \propto J_{ij}\mathbf{S}_i\mathbf{S}_j + K_{ij}\tau_i\tau_j$, where K_{ij} represents orbital-orbital exchange interactions, and the corresponding phonon renormalization also involves the orbital effect. It is to be noted that this renormalized temperature scale is in line with an anomalous broad feature observed at ~ 40 K in earlier thermal conductivity studies of an analogous TLAF candidate $\text{Ba}_3\text{CoSb}_2\text{O}_9$, where it has been associated with the presence of strong magnetic fluctuations due to the frustration of Co spins [68]. Such strong quantum fluctuation until very high temperature may be the reflection of the underlying frustration of Ni^{2+} spins on the triangular lattice in $\text{Ca}_3\text{NiNb}_2\text{O}_9$. We note that similar phonon-mode softening and linewidth broadening were also reported for a QSL candidate Cu_2IrO_3 , attributed to the strong coupling of phonons with the Majorana fermions [51], evidencing the spin fractionalization in Cu_2IrO_3 . The anomalies observed in our measurements for the phonon modes may have their origin in the coupling of phonons with the underlying Majorana fermions. We note that some of the mode frequencies and FWHMs show a change in slope at T^* (~ 200 K). A complete understanding about these transitions requires more theoretical and experimental studies, and we hope that our results will provide the required stimulation.

To understand the symmetry of the observed phonon modes, we also performed polarization-dependent Raman measurements. We did our measurements for two scattering configurations, namely, $(\theta\theta_0)$ and $(\theta\theta)$. In the $(\theta\theta_0)$ configuration, incident light polarization is rotated using a polarizer ($\lambda/2$ plate) in steps of 20° from 0° to 360° , while the scattered light polarization is fixed parallel to the Y axis using an analyzer. The $(\theta\theta)$ polarization configuration involves the simultaneous rotation of the polarizer and analyzer such that the incident light and scattered light are always parallel, i.e., $\hat{e}_i//\hat{e}_s$. Figure 6(a) shows the polarized Raman spectra for both configurations at 8 and 330 K. Detailed theoretical descriptions of the phonons mode intensity with A_g and B_g symmetry as per group theory in these two polarization configurations are given in detail in Sec. S4 in the Supplemental Material [40], and the experimental data in both these configurations as well as at two temperature (8 and 330 K) are shown in Figs. S4 and S5 in the Supplemental Material [40]. In the $(\theta\theta_0)$ configuration, phonon modes with A_g and B_g symmetry show twofold symmetry, i.e., maxima at two angles. However, the $(\theta\theta)$ configuration modes with B_g symmetry change to fourfold symmetry, i.e., maxima at four angles. Therefore, modes where twofold symmetry remains similar in these two polarization configurations are attributed with A_g symmetry, e.g., see mode P16 in Fig. 6(c). On the other hand, modes which change from twofold to fourfold symmetry when going from $(\theta\theta_0)$ to $(\theta\theta)$ configurations are attributed with B_g symmetry, e.g., see mode P18 in Fig. 6(c). Additionally, we observed some modes which show quasi-isotropic behavior in $(\theta\theta_0)$ polarization

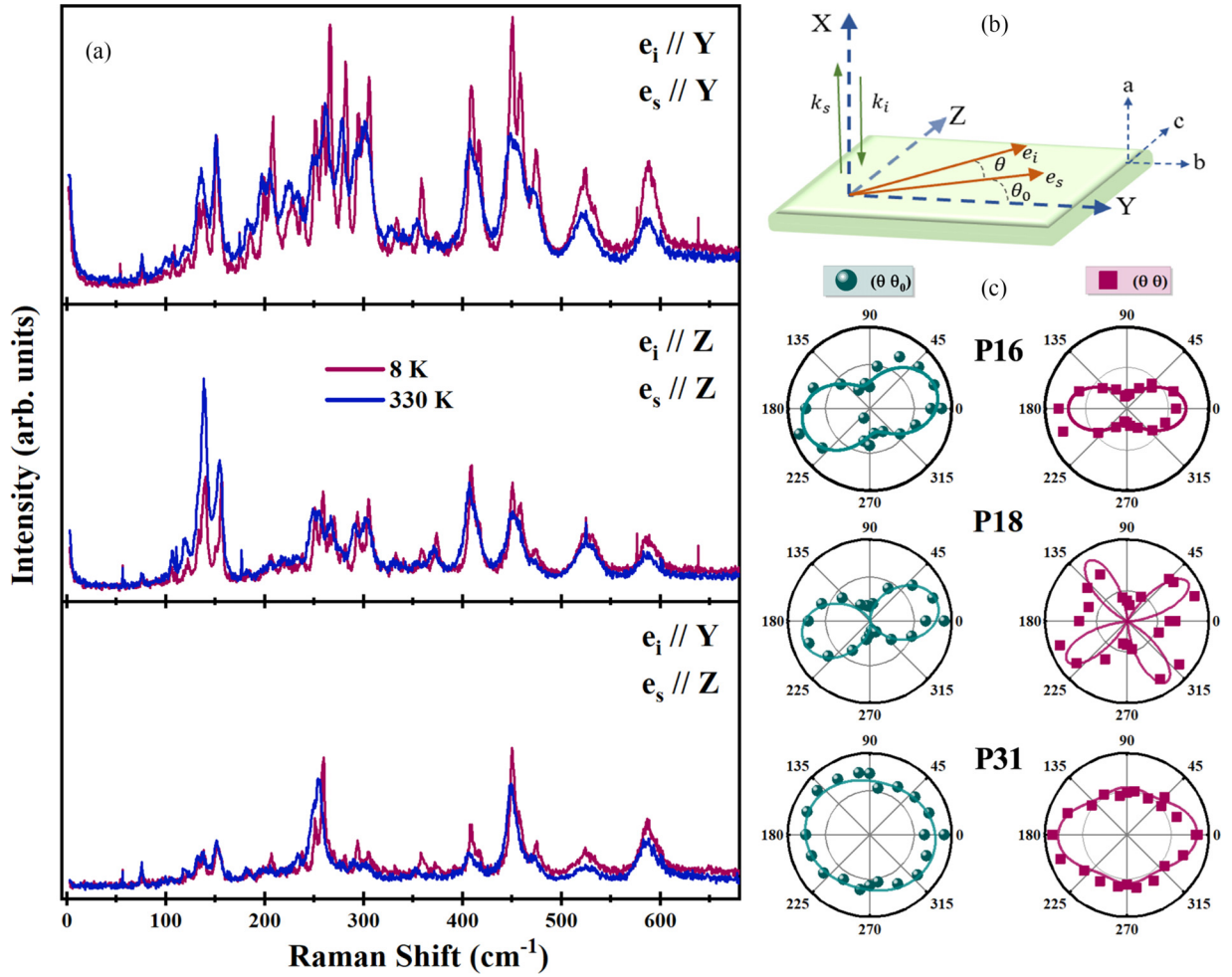


FIG. 6. (a) Comparison of the Raman spectra of $\text{Ca}_3\text{NiNb}_2\text{O}_9$ at 8 and 330 K taken under different polarization configurations from the bc plane. (b) Plane projection of the polarization direction of the incident and scattered light, (c) P16, P18 and P31 phonon mode polarization-dependent intensities for both configurations at 8 K [green data for $(\theta\theta_0)$ and red data plot for $(\theta\theta)$ configurations]. The solid curves are fitted with angular-dependence mode intensity equations as described in Sec. S4 in the Supplemental Material [40].

configuration, and changes to weak fourfold symmetry are attributed to the combined A_g and B_g symmetries, e.g., see mode P31 in Fig. 6(c). Table S2 in the Supplemental Material [40] provides the symmetry assignment of the observed phonon modes based on our in-depth polarization-dependent measurements.

IV. CONCLUSIONS

We report on a detailed temperature-dependent Raman spectroscopic study on single crystals of frustrated TLAF $\text{Ca}_3\text{NiNb}_2\text{O}_9$. We observed the continuum with anomalous temperature evolution, suggesting its origin in the possible exotic magnetic excitations which might be due to fractionalization of Ni^{2+} spins on the frustrated triangular lattice. The phonon profiles exhibit Fano asymmetries indicative of coupling to a magnetic continuum well above the long-range magnetic ordering temperature. Self-energy parameters of the phonons and the background continuum reveal two unusual

transitions at $T_{\text{SC}} \sim 50$ K and $T^* \sim 200$ K; the former is attributed to the possible spin and orbital fluctuations. As the temperature reaches T_{SC} , there is a significant redistribution of spectral weight at the demarcating Raman shift $\omega_F \sim 203 \text{ cm}^{-1}$ also reflected in the anomalous phonon-mode intensity evolution. Our observations suggests that $\text{Ca}_3\text{NiNb}_2\text{O}_9$ lies in close proximity to the QSL state. The spin $S = 1$ Ni^{2+} -based TLAF systems remain a field of active investigation. Phenomena for the emergence of spin-correlated phases are still not fully understood. Therefore, our findings will inspire future advanced experimental exposure and theoretical modeling, which may contribute to the exploration of spin-liquid states of frustrated magnetic materials.

ACKNOWLEDGMENT

P.K. acknowledges support from IIT Mandi for the experimental facilities and financial support from SERB (Grant No. CRG/2023/002069) India.

- [1] L. Balents, Spin liquids in frustrated magnets, *Nature (London)* **464**, 199 (2010).
- [2] C. Broholm, R. J. Cava, S. A. Kivelson, D. G. Nocera, M. R. Norman, and T. Senthil, Quantum spin liquids, *Science* **367**, 263 (2020).
- [3] V. R. Shaginyan, V. A. Stephanovich, A. Z. Msezane, G. S. Japaridze, J. W. Clark, M. Y. Amusia, and E. V. Kirichenko, Theoretical and experimental developments in quantum spin liquid in geometrically frustrated magnets: A review, *J. Mater. Sci.* **55**, 2257 (2020).
- [4] J. Wen, S. L. Yu, S. Li, W. Yu, and J. X. Li, Experimental identification of quantum spin liquids, *npj Quantum Mater.* **4**, 12 (2019).
- [5] C. Nayak, S. H. Simon, A. Stern, M. Freedman, and S. Das Sarma, Non-Abelian anyons and topological quantum computation, *Rev. Mod. Phys.* **80**, 1083 (2008).
- [6] X. G. Wen, Quantum orders and symmetric spin liquids, *Phys. Rev. B* **65**, 165113 (2002).
- [7] P. W. Anderson, Resonating valence bonds: A new kind of insulator? *Mater. Res. Bull.* **8**, 153 (1973).
- [8] T. H. Han, J. S. Helton, S. Chu, D. G. Nocera, J. A. Rodriguez-Rivera, C. Broholm, and Y. S. Lee, Fractionalized excitations in the spin-liquid state of a kagome-lattice antiferromagnet, *Nature (London)* **492**, 406 (2012).
- [9] H. D. Zhou, C. Xu, A. M. Hallas, H. J. Silverstein, C. R. Wiebe, I. Umegaki, J. Q. Yan, T. P. Murphy, J. Park, Y. Qiu *et al.*, Successive phase transitions and extended spin-excitation continuum in the $S = \frac{1}{2}$ triangular-lattice antiferromagnet $\text{Ba}_3\text{CoSb}_2\text{O}_9$, *Phys. Rev. Lett.* **109**, 267206 (2012).
- [10] Y. Shen, Y. D. Li, H. C. Walker, P. Steffens, M. Boehm, X. Zhang, S. Shen, H. Wo, G. Chen, and J. Zhao, Fractionalized excitations in the partially magnetized spin liquid candidate YbMgGaO_4 , *Nat. Commun.* **9**, 4138 (2018).
- [11] T. Dey, A. V. Mahajan, P. Khuntia, M. Baenitz, B. Koteswararao, and F. C. Chou, Spin-liquid behavior in $J_{\text{eff}} = \frac{1}{2}$ triangular lattice compound $\text{Ba}_3\text{IrTi}_2\text{O}_9$, *Phys. Rev. B* **86**, 140405(R) (2012).
- [12] S. Lal, S. J. Sebastian, S. S. Islam, M. P. Saravanan, M. Uhlarz, Y. Skourski, and R. Nath, Double magnetic transitions and exotic field-induced phase in the triangular lattice antiferromagnets $\text{Sr}_3\text{Co}(\text{Nb}, \text{Ta})_2\text{O}_9$, *Phys. Rev. B* **108**, 014429 (2023).
- [13] S. Kundu, A. Shahee, A. Chakraborty, K. M. Ranjith, B. Koo, J. Sichelschmidt, M. T. F. Telling, P. K. Biswas, M. Baenitz, I. Dasgupta *et al.*, Gapless quantum spin liquid in the triangular system $\text{Sr}_3\text{CuSb}_2\text{O}_9$, *Phys. Rev. Lett.* **125**, 267202 (2020).
- [14] Z. Lu, L. Ge, G. Wang, M. Russina, G. Günther, C. R. dela Cruz, R. Sinclair, H. D. Zhou, and J. Ma, Lattice distortion effects on the frustrated spin-1 triangular-antiferromagnet $\text{A}_3\text{NiNb}_2\text{O}_9$ ($A = \text{Ba}, \text{Sr}, \text{and Ca}$), *Phys. Rev. B* **98**, 094412 (2018).
- [15] A. V. Chubukov, S. Sachdev, and T. Senthil, Large- S expansion for quantum antiferromagnets on a triangular lattice, *J. Phys.: Condens. Matter* **6**, 8891 (1994).
- [16] T. Susuki, N. Kurita, T. Tanaka, H. Nojiri, A. Matsuo, K. Kindo, and H. Tanaka, Magnetization process and collective excitations in the $S = \frac{1}{2}$ triangular-lattice Heisenberg antiferromagnet $\text{Ba}_3\text{CoSb}_2\text{O}_9$, *Phys. Rev. Lett.* **110**, 267201 (2013).
- [17] M. Lee, J. Hwang, E. S. Choi, J. Ma, C. R. dela Cruz, M. Zhu, X. Ke, Z. L. Dun, and H. D. Zhou, Series of phase transitions and multiferroicity in the quasi-two-dimensional spin- $\frac{1}{2}$ triangular-lattice antiferromagnet $\text{Ba}_3\text{CoNb}_2\text{O}_9$, *Phys. Rev. B* **89**, 104420 (2014).
- [18] D. Rout, R. Tang, M. Skoulatos, B. Ouladdiaf, Y. Kinoshita, A. Miyake, M. Tokunaga, S. Mahapatra, and S. Singh, Ordered and disordered variants of the triangular lattice antiferromagnet $\text{Ca}_3\text{NiNb}_2\text{O}_9$: Crystal growth and magnetic properties, *Phys. Rev. Mater.* **7**, 024419 (2023).
- [19] J. Hwang, E. S. Choi, F. Ye, C. R. dela Cruz, Y. Xin, H. D. Zhou, and P. Schlottmann, Successive magnetic phase transitions and multiferroicity in the spin-one triangular-lattice antiferromagnet $\text{Ba}_3\text{NiNb}_2\text{O}_9$, *Phys. Rev. Lett.* **109**, 257205 (2012).
- [20] M. Serbyn, T. Senthil, and P. A. Lee, Exotic $S = 1$ spin-liquid state with fermionic excitations on the triangular lattice, *Phys. Rev. B* **84**, 180403(R) (2011).
- [21] G. Chen, M. Hermele, and L. Radzihovsky, Frustrated quantum critical theory of putative spin-liquid phenomenology in $6H\text{-B-Ba}_3\text{NiSb}_2\text{O}_9$, *Phys. Rev. Lett.* **109**, 016402 (2012).
- [22] S. Jeon, D. Wulferding, Y. Choi, S. Lee, K. Nam, K. H. Kim, M. Lee, T.-H. Jang, J.-H. Park, S. Lee *et al.*, One-ninth magnetization plateau stabilized by spin entanglement in a kagome antiferromagnet, *Nat. Phys.* **20**, 435 (2024).
- [23] Y. Shirata, H. Tanaka, A. Matsuo, and K. Kindo, Experimental realization of a spin- $\frac{1}{2}$ triangular-lattice Heisenberg antiferromagnet, *Phys. Rev. Lett.* **108**, 057205 (2012).
- [24] Q. Huang, M. Lee, E. S. Choi, J. Ma, C. dela Cruz, and H. D. Zhou, Successive phase transitions and multiferroicity in deformed triangular-lattice antiferromagnets $\text{Ca}_3\text{MnNb}_2\text{O}_9$ ($M = \text{Co}, \text{Ni}$) with spatial anisotropy, *ECS J. Solid State Sci. Technol.* **11**, 063004 (2022).
- [25] K. W. Plumb, J. P. Clancy, L. J. Sandilands, V. V. Shankar, Y. F. Hu, K. S. Burch, H. Y. Kee, and Y. J. Kim, $\alpha\text{-RuCl}_3$: A spin-orbit assisted Mott insulator on a honeycomb lattice, *Phys. Rev. B* **90**, 041112(R) (2014).
- [26] L. J. Sandilands, Y. Tian, K. W. Plumb, Y. Kim, and K. S. Burch, Scattering continuum and possible fractionalized excitations in $\alpha\text{-RuCl}_3$, *Phys. Rev. Lett.* **114**, 147201 (2015).
- [27] V. Kumar, D. Kumar, B. Singh, Y. Shemerliuk, M. Behnami, B. Büchner, S. Aswartham, and P. Kumar, Fluctuating fractionalized spins in quasi-two-dimensional magnetic $\text{V}_{0.85}\text{PS}_3$, *Phys. Rev. B* **107**, 094417 (2023).
- [28] B. Singh, D. Kumar, V. Kumar, M. Vogl, S. Wurmehl, S. Aswartham, B. Büchner, and P. Kumar, Fractional spin fluctuations and quantum liquid signature in $\text{Gd}_2\text{ZnIrO}_6$, *Phys. Rev. B* **104**, 134402 (2021).
- [29] H. Kawamura, Spin-wave analysis of the antiferromagnetic plane rotator model on the triangular lattice-symmetry breaking in magnetic field, *J. Phys. Soc. Jpn.* **53**, 2452 (1984).
- [30] M. Yun and G. S. Jeon, Classical Heisenberg antiferromagnet on a triangular lattice in the presence of single-ion anisotropy, *J. Phys.: Conf. Ser.* **592**, 012111 (2015).
- [31] Y. Choi, S. Lee, J. H. Lee, S. Lee, M. J. Seong, and K. Y. Choi, Bosonic spinons in anisotropic triangular antiferromagnets, *Nat. Commun.* **12**, 6453 (2021).
- [32] J. Nasu, J. Knolle, D. L. Kovrizhin, Y. Motome, and R. Moessner, Fermionic response from fractionalization in an insulating two-dimensional magnet, *Nat. Phys.* **12**, 912 (2016).
- [33] B. Singh, M. Vogl, S. Wurmehl, S. Aswartham, B. Büchner, and P. Kumar, Kitaev magnetism and fractionalized excitations in double perovskite $\text{Sm}_2\text{ZnIrO}_6$, *Phys. Rev. Res.* **2**, 013040 (2020).

- [34] P. Lemmens, G. Güntherodt, and C. Gros, Magnetic light scattering in low-dimensional quantum spin systems, *Phys. Rep.* **375**, 1 (2003).
- [35] D. Kumar, V. Kumar, R. Kumar, M. Kumar, and P. Kumar, Electron-phonon coupling, thermal expansion coefficient, resonance effect, and phonon dynamics in high-quality CVD-grown monolayer and bilayer MoSe₂, *Phys. Rev. B* **105**, 085419 (2022).
- [36] M. E. Valentine, S. Koohpayeh, M. Mourigal, T. M. McQueen, C. Broholm, and N. Drichko, Raman study of magnetic excitations and magnetoelastic coupling in α -SrCr₂O₄, *Phys. Rev. B* **91**, 144411 (2015).
- [37] Y. Fu, M. L. Lin, L. Wang, Q. Liu, L. Huang, W. Jiang, Z. Hao, C. Liu, H. Zhang, X. Shi *et al.*, Dynamic fingerprint of fractionalized excitations in single-crystalline Cu₃Zn(OH)₆FBr, *Nat. Commun.* **12**, 3048 (2021).
- [38] A. Baum, H. N. Ruiz, N. Lazarevic, Y. Wang, T. Bohm, R. H. Ahangharnejhad, A. Adelman, T. Wolf, Z. V. Popovic, B. Moritz *et al.*, Frustrated spin order and stripe fluctuations in FeSe, *Nat. Commun.* **2**, 14 (2019).
- [39] D. L. Rousseau, R. P. Bauman, and S. P. S. Porto, Normal mode determination in crystals, *J. Raman Spectrosc.* **10**, 253 (1981).
- [40] See Supplemental Material at <http://link.aps.org/supplemental/10.1103/PhysRevB.110.024430> for discussions about the experimental techniques, anharmonic phonon-phonon interaction model, Raman spectra of ordered and disordered crystal, and temperature and polarization analysis of the phonons, which also contains Refs. [18,35,60,65,69–72].
- [41] H. Wang, R. Fu, X. Liu, Y. Xu, and Y. Liu, Low temperature sintered of Ba₃MgNb₂O₉ ceramics with high quality factor via B-site oxide precursor method, *J. Mater. Sci. Mater. Electron.* **31**, 20245 (2020).
- [42] A. P. Kampf and W. Breinig, Raman scattering from antiferromagnetic spin fluctuations, *Z. Phys. B* **89**, 313 (1992).
- [43] L. Testa, V. Šurija, K. Prša, P. Steffens, M. Boehm, P. Bourges, H. Berger, B. Normand, H. M. Rønnow, and I. Živković, Triplons, magnons, and spinons in a single quantum spin system: SeCuO₃, *Phys. Rev. B* **103**, L020409 (2021).
- [44] A. Mezio, L. O. Manuel, R. R. P. Singh, and A. E. Trumper, Low temperature properties of the triangular-lattice antiferromagnet: A Bosonic spinon theory, *New J. Phys.* **14**, 123033 (2012).
- [45] A. Glamazda, P. Lemmens, S.-H. Do, Y. S. Choi, and K. Y. Choi, Raman spectroscopic signature of fractionalized excitations in the harmonic-honeycomb iridates β - and γ -Li₂IrO₃, *Nat. Commun.* **7**, 12286 (2016).
- [46] C. Xu, F. Wang, Y. Qi, L. Balents, and M. P. A. Fisher, Spin liquid phases for spin-1 systems on the triangular lattice, *Phys. Rev. Lett.* **108**, 087204 (2012).
- [47] B. Fåk, S. Bieri, E. Canévet, L. Messio, C. Payen, M. Viaud, C. Guillot-Deudon, C. Darie, J. Ollivier, and P. Mendels, Evidence for a spinon Fermi surface in the triangular $S = 1$ quantum spin liquid Ba₃NiSb₂O₉, *Phys. Rev. B* **95**, 060402(R) (2017).
- [48] J. G. Cheng, G. Li, L. Balicas, J. S. Zhou, J. B. Goodenough, C. Xu, and H. D. Zhou, High-pressure sequence of Ba₃NiSb₂O₉ structural phases: New $S = 1$ quantum spin liquids based on Ni²⁺, *Phys. Rev. Lett.* **107**, 197204 (2011).
- [49] K. Feng, S. Swarup, and N. B. Perkins, Footprints of Kitaev spin liquid in the Fano lineshape of Raman-active optical phonons, *Phys. Rev. B* **105**, L121108 (2022).
- [50] A. Metavitsiadis, W. Natori, J. Knolle, and W. Brenig, Optical phonons coupled to a Kitaev spin liquid, *Phys. Rev. B* **105**, 165151 (2022).
- [51] S. Pal, A. Seth, P. Sakrikar, A. Ali, S. Bhattacharjee, D. V. S. Muthu, Y. Singh, and A. K. Sood, Probing signatures of fractionalization in the candidate quantum spin liquid Cu₂IrO₃ via anomalous Raman scattering, *Phys. Rev. B* **104**, 184420 (2021).
- [52] D. Wulferding, Y. Choi, S. Do, C. H. Lee, P. Lemmens, C. Faugeras, Y. Gallais, and K. Choi, Magnon bound states versus anyonic Majorana excitations in the Kitaev honeycomb magnet, *Nat. Commun.* **11**, 1603 (2020).
- [53] D. Lin, K. Ran, H. Zheng, J. Xu, L. Gao, J. Wen, S. Yu, J. Li, and X. Xi, Anisotropic scattering continuum induced by crystal symmetry reduction in atomically thin α -RuCl₃, *Phys. Rev. B* **101**, 045419 (2020).
- [54] E. H. Hasdeo, A. R. T. Nugraha, M. S. Dresselhaus, and R. Saito, Breit-Wigner-Fano line shapes in Raman spectra of graphene, *Phys. Rev. B* **90**, 245140 (2014).
- [55] U. Fano, Effects of configuration interaction on intensities and phase shifts, *Phys. Rev.* **124**, 1866 (1961).
- [56] A. Glamazda, P. Lemmens, S. Do, Y. S. Kwon, and K. Y. Choi, Relation between Kitaev magnetism and structure in α -RuCl₃, *Phys. Rev. B* **95**, 174429 (2017).
- [57] J. Yoshitake, J. Nasu, and Y. Motome, Fractional spin fluctuations as a precursor of quantum spin liquids: Majorana dynamical mean-field study for the Kitaev model, *Phys. Rev. Lett.* **117**, 157203 (2016).
- [58] J. Nasu, M. Udagawa, and Y. Motome, Vaporization of Kitaev spin liquids, *Phys. Rev. Lett.* **113**, 197205 (2014).
- [59] G. Li, L. L. Huang, X. Chen, C. Liu, S. Pei, X. Wang, S. Wang, Y. Zhao, D. Yu, L. Wang *et al.*, Relation between Kitaev magnetism and structure in α -RuCl₃, *Phys. Rev. B* **101**, 174436 (2020).
- [60] M. Cardona and G. Güntherodt, *Light Scattering in Solid II* (Springer, Berlin, 1982).
- [61] M. Greiter and R. Thomale, Non-Abelian statistics in a quantum antiferromagnet, *Phys. Rev. Lett.* **102**, 207203 (2009).
- [62] T. R. Hart, R. L. Aggarwal, and B. Lax, Temperature dependence of Raman scattering in silicon, *Phys. Rev. B* **1**, 638 (1970).
- [63] B. Singh, G. A. Cansever, T. Dey, A. Maljuk, S. Wurmehl, B. Buchner, and P. Kumar, Orbital-phonon coupling in Ir⁵⁺ ($5d^4$) double perovskite Ba₂YIrO₆, *J. Phys.: Condens. Matter* **31**, 065603 (2019).
- [64] M. Cardona and T. Ruf, Phonon self-energies in semiconductors: Anharmonic and isotopic contributions, *Solid State Commun.* **117**, 201 (2001).
- [65] P. G. Klemens, Anharmonic decay of optical phonons, *Phys. Rev.* **148**, 845 (1966).
- [66] S. Pal, A. Seth, A. Ali, Y. Singh, D. V. S. Muthu, S. Bhattacharjee, and A. K. Sood, Strong coupling of lattice

- and orbital excitations in the quantum magnet $\text{Ca}_{10}\text{Cr}_7\text{O}_{28}$: Anomalous temperature dependence of Raman phonons, *Phys. Rev. B* **108**, L241103 (2023).
- [67] E. Granado, A. García, J. A. Sanjurjo, C. Rettori, I. Torriani, F. Prado, R. D. Sánchez, A. Caneiro, and S. B. Oseroff, Magnetic ordering effects in the Raman spectra of $\text{La}_{1-x}\text{Mn}_{1-x}\text{O}_3$, *Phys. Rev. B* **60**, 11879 (1999).
- [68] K. Naruse, T. Kawamata, M. Ohno, Y. Matsuoka, H. Sudo, H. Nagasawa, Y. Hagiya, T. Sasaki, and Y. Koike, Thermal conductivity in the triangular-lattice antiferromagnet $\text{Ba}_3\text{CoSb}_2\text{O}_9$, *J. Phys. Conf. Ser.* **568**, 042014 (2014).
- [69] I. P. Ipatova, A. A. Maradudin, and R. F. Wallis, Temperature dependence of the width of the fundamental lattice-vibration absorption peak in ionic crystals. II. Approximate numerical results, *Phys. Rev.* **155**, 882 (1967).
- [70] M. Balkanski, R. F. Wallis, and E. Haro, Anharmonic effects in light scattering due to optical phonons in silicon, *Phys. Rev. B* **28**, 1928 (1983).
- [71] F. Albert Cotton, *Chemical Applications of Group Theory* (Wiley-Interscience, New York, 1990).
- [72] R. Loudon, The Raman effect in crystals, *Adv. Phys.* **13**, 423 (1964).